IX International Conference on Computational Methods in Marine Engineering
MARINE 2021
I.M. Viola and F. Brennan (Eds)

A QUASI-MONTE CARLO VOLUME INTEGRATION AND CHEBYSHEV PICARD ITERATION METHOD FOR TIME-PARALLEL NONLINEAR SEAKEEPING COMPUTATIONS

DAVID F. H. LARSON AND PAUL D. SCLAVOUNOS

Massachusetts Institute of Technology
Cambridge, Massachusetts
e-mail: dflarson@mit.edu and pauls@mit.edu

Key words: implicit geometry, Quasi-Monte Carlo, Picard iteration, seakeeping

Abstract. The design and analysis of vessels and wave energy converters requires an understanding of the nonlinear loads and responses in stochastic waves. A novel mesh-free potential flow methodology is introduced for simulating the response of a floating body with nonlinear Froude-Krylov and hydrostatic effects. The nonlinear fluid forces are cast as volume integrals using Fluid Impulse Theory (FIT). These volume integrals are robustly evaluated using Quasi-Monte Carlo (QMC) integration over an implicit geometry without the need to discretize the hull or free surfaces. The resulting nonlinear equation of motion is solved with an impulse-adapted Chebyshev Picard iteration scheme (I-MCPI). By approximating the nonlinear momentum impulse with a Chebyshev series, the time derivative can be analytically computed, circumventing the numerical sensitivity of finite-differencing. The solution is shown to converge over short parallelized subintervals, and sequentially concatenated to form long time records.

1 INTRODUCTION

The last decade has seen a significant development of high-fidelity computational methods for marine hydrodynamics and seakeeping. Despite these advances, computationally-efficient potential flow methods capable of capturing the dominant nonlinearities remain invaluable for design optimization and analysis tasks that require ensembles of simulations over broad parameter spaces. The dominant potential flow hydrodynamic nonlinearities in moderate conditions are the incident wave Froude-Krylov and hydrostatic effects.

While there are many approaches to modeling the nonlinear Froude-Krylov and hydrostatic effects, they are not without compromises. The primary source of computational effort arises from the computation of the instantaneous wetted body surface [1]. For general bodies requiring a discrete mesh-mesh intersection, this is well-known to be a numerically sensitive and challenging task [2]. For this reason, two-dimensional and strip theory codes for ship seakeeping analysis have remained robust and useful, despite the simplification of the ship hydrodynamics [3]. Efficient and robust three dimensional analytic expressions of the nonlinear hydrodynamic force

integrals have been developed recently for wave energy converters, but are limited to axisymmetric body surfaces [4].

Even with geometric simplifications or robust forces, these equations of motion can be challenging to advance robustly in time. Small time steps needed for stability and accuracy can lead to prohibitively long simulation times. In particular, time derivatives may introduce noise or instability, leading to some to introduce auxiliary potentials to circumvent temporal differentiation [5].

A new perspective for addressing these challenges is introduced in this work. Expressions for the dominant Froude-Krylov and hydrostatic nonlinearities over the instantaneous submerged volume are developed using FIT. The loads are numerically evaluated by a robust QMC integration scheme over the blurred-boundary signed distance function (SDF) representation of an arbitrary body geometry. This scheme avoids discretizing any surfaces, circumventing numerically-sensitive mesh-mesh intersections. A Chebyshev Picard algorithm is developed to robustly differentiate the nonlinear fluid impulses and evolve the simulation forward in time. The convergence and sensitivity behavior of this method is discussed.

2 METHODOLOGY

The geometry is described in a body-fixed coordinate system (BCS) $\boldsymbol{x} \equiv (x, y, z)$, whose origin at rest design conditions is centered vertically on the calm-water plane. The displacement of the BCS is defined with respect to an inertial global coordinate system (GCS) $\boldsymbol{X} \equiv (X, Y, Z)$ by a displacement vector $\boldsymbol{\xi}$. The equation of motion is given by Newton's Law, which for this study, is simplified to translation only,

$$M\ddot{\boldsymbol{\xi}} = \boldsymbol{F}_{FK} + \boldsymbol{F}_{Hs} + \boldsymbol{F}_{\text{Rad}} + \boldsymbol{F}_{\text{Diff}} + \boldsymbol{F}_{\text{gravity}} \tag{1}$$

2.1 Fluid Impulse Theory Hydrodynamic Forces

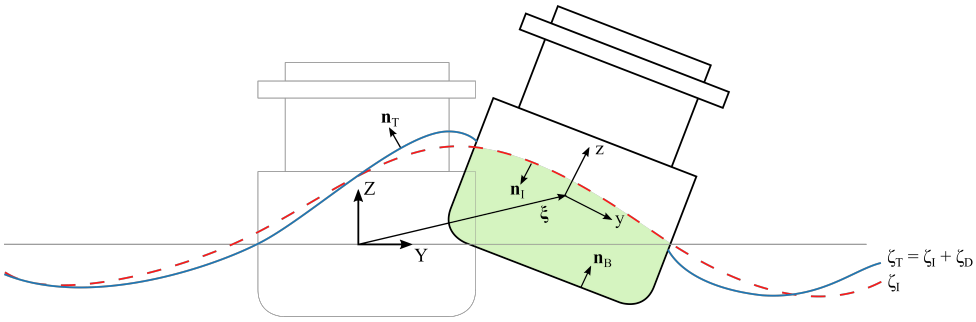

Figure 1: A body experiencing large amplitude response motions in irregular waves. The total nonlinear free surface ζ_T is denoted with the solid blue curve, while the incident wave free surface ζ_I is denoted by the dashed red curve. S_B is the exact instantaneous wetted body surface bound by ζ_T, while S_W is the wetted body surface bounded by the incident wave free surface. S_I is the incident wave free surface interior to the body and S_E is the incident wave surface exterior to the body.

Assuming the fluid is inviscid and the flow is incompressible and irrotational, the fluid velocity can be defined as the gradient of a scalar velocity potential $\boldsymbol{v} \equiv \nabla\Phi$. The nonlinear fluid forces acting on a body undergoing large amplitude motions are expressed as the time derivative of the velocity potential integrated over the instantaneous wetted surface,

$$-\rho \int\limits_{S_B} \left[\frac{\partial \Phi}{\partial t} + \frac{1}{2}\nabla\Phi \cdot \nabla\Phi + gZ\right] \boldsymbol{n}\mathrm{d}s = -\rho \frac{d}{dt} \int\limits_{S_B+S_T} \Phi \boldsymbol{n}\mathrm{d}s - \rho g \int\limits_{S_B+S_T} Z\boldsymbol{n}\mathrm{d}s \tag{2}$$

The left hand side of equation (2) is the integral of the Bernoulli pressure over the instantaneous wetted body surface. The total velocity potential Φ can be decomposed into the incident wave potential, and the diffraction and radiation disturbances, $\Phi = \phi_I + \phi_D$. The incident wave represented by a superposition of deep water regular waves with amplitudes drawn from a spectrum and uniform random phases, and Wheeler stretching is employed to extend the wave kinematics above the $Z = 0$ plane [6]. The total force is decomposed accordingly, (see [7] for details),

$$\begin{aligned} \boldsymbol{F} = &- \rho g \int\limits_{S_W+S_I} Z\boldsymbol{n}\mathrm{d}s - \rho \frac{d}{dt} \int\limits_{S_W+S_I} \phi_I \boldsymbol{n}\mathrm{d}s - \rho \frac{d}{dt} \int\limits_{S_W} \phi_D \boldsymbol{n}\mathrm{d}s \\ &- \rho \frac{d}{dt} \int\limits_{S_T+\Delta S} \phi_D \boldsymbol{n}\mathrm{d}s - \rho \frac{d}{dt} \int\limits_{S_T+\Delta S+S_E} \phi_I \boldsymbol{n}\mathrm{d}s - \rho g \int\limits_{S_T+\Delta S+S_E} Z\boldsymbol{n}\mathrm{d}s \end{aligned} \tag{3}$$

The integration surfaces are depicted in Figure (1), and ΔS is the differential surface between S_B and S_W.

In this model, the nonlinear Froude-Krylov and hydrostatic effects are assumed to be the dominant nonlinearities, which are represented by the first and second terms on the right-hand side of (3), respectively. The surface integrals in defining these two components are defined over the closed wetted surface formed by the intersection of the body and incident wave surfaces. By virtue of Gauss's theorem, the nonlinear hydrostatic and FK components can be expressed as volume integrals,

$$\boldsymbol{F}_{Hs} = \rho g \int\limits_{\forall_W} 1\, \hat{k}\, \mathrm{d}v = \rho g \forall_W(t)\, \hat{k} \tag{4a}$$

$$\boldsymbol{F}_{FK} = \rho \frac{d}{dt} \int\limits_{\forall_W} \nabla\phi_I \mathrm{d}v \tag{4b}$$

where $\forall_W(t)$ is the instantaneous wetted volume bounded by $S_W + S_I$. This transformation yields an intuitive nonlinear generalization of Archimedean hydrostatics.

The radiation and diffraction body disturbances are contained in the third term of equation (3). A fully nonlinear treatment, comes with a considerable increase in computational complexity. As such, the body disturbances will be assumed to be small and approximated as linear.

The linear frequency-dependent response of the radiation component is expressed in the time domain via the Cummins impulse response convolution [8],

$$F_{\text{Rad}} = -A_\infty \ddot{\xi} - \int_{-\infty}^{t} \kappa\left(t-\tau\right)\dot{\xi}\left(\tau\right)\mathrm{d}\tau \tag{5}$$

where $A_{\infty,ij} = A_{ij}(\omega \to \infty)$ is the infinite frequency added mass, and the impulse response kernel $\kappa(\tau)$ can be computed from the linear added mass and damping coefficients provided by any linear panel code, e.g. WAMIT [9]. Details of the implementation can be found in [10].

The corresponding linear diffraction problem results in a set of complex-valued coefficients $\mathbb{X}_{D,i}\left(\omega\right)$, and the corresponding linear diffraction force in terms of an incident sinusoidal wave of amplitude A and frequency ω may be evaluated directly as,

$$F_{\text{Diff}} = \left|\mathbb{X}_{\text{Diff}}\left(\omega\right)\right| \sin\left[\omega t + \frac{\Im\left\{\mathbb{X}_{\text{Diff}}\left(\omega\right)\right\}}{\Re\left\{\mathbb{X}_{\text{Diff}}\left(\omega\right)\right\}}\right] \tag{6}$$

The fourth, fifth, and sixth terms in equation (3) are the free surface impulses which are neglected under the small-disturbance assumption.

2.2 Implicit Surface Representation

The first step in the numerical computation of the nonlinear forces (4) is to evaluate the bounds of the volume integrals, which involves an intersection between the instantaneous body position and the ambient wave free surface. The implicit surface $\mathcal{S}$ is defined as the zero level set of a scalar function, which leads to a convenient behavior that the sign of the function changes across the boundary [11]. The benefit of the implicit surface approach is that it immediately determines whether a point $\boldsymbol{p}$ is inside or outside the enclosing surface $\mathcal{S}$. Therefore, set operations such as unions and intersections are straightforward.

$$\mathcal{I}_\forall\left(\boldsymbol{p}\right) = \begin{cases} 1 & D_{\mathcal{S}}\left(\boldsymbol{p}\right) \leq 0 \\ 0 & D_{\mathcal{S}}\left(\boldsymbol{p}\right) > 0 \end{cases} \tag{7}$$

A special level set function is the signed distance function, denoted as $D_{\mathcal{S}}\left(\boldsymbol{p}\right)$ which is employed here. The magnitude of $D_{\mathcal{S}}$ evaluated at $\boldsymbol{p}$ is the shortest Euclidean distance from $\boldsymbol{p}$ to the surface $\mathcal{S}$ (visualized for a circle and square in Figure 2). The SDF for useful primitive shapes, such as spheres, cylinders, prisms and cones, exist in closed analytical form which are common in marine engineering applications. SDFs can also be constructed from general discrete mesh geometries thereby enabling the broader extension of this approach to complex body shapes [11].

2.3 Quasi-Monte Carlo Integration

It is well known that in the deterministic sense, numerically integrating a function over a definite volume is more expensive than integrating the corresponding surface integral transformed via Gauss's Theorem. Quasi-Monte Carlo integration (QMC) [12] is employed to both relieve this curse of dimensionality and leverage the implicit geometry representation.

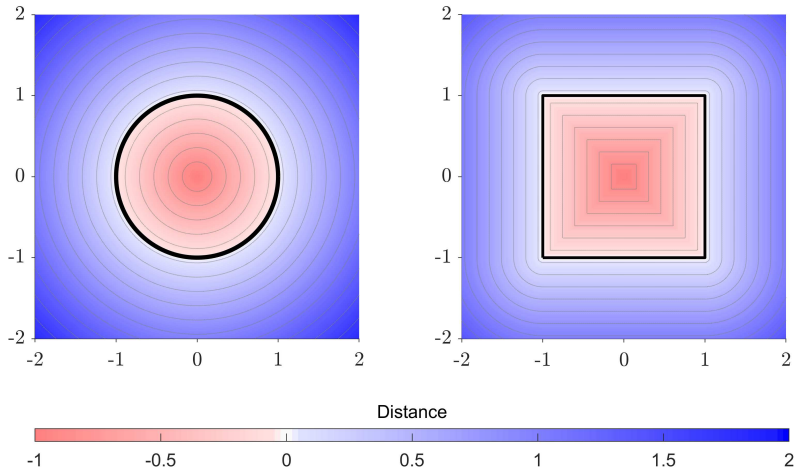

Figure 2: Contours of a signed distance function of a circle $D_{\text{circle}}(\boldsymbol{p}) = \sqrt{\boldsymbol{p}\cdot\boldsymbol{p}} - R$ and square $D_{\text{square}}(\boldsymbol{p}) = \sqrt{\max(0,q_1)^2 + \max(0,q_2)^2} + \min(0,\max(q_1,q_2))$ with $\boldsymbol{q} = |\boldsymbol{p}| - L/2$ and side length L.

The classical Monte Carlo integration (MC) invokes the insignt that the expectation operator is simply an integration operator over a domain, which can be approximated as a statistical average of N samples of the integrand,

$$I = \int_{\Omega} f(\boldsymbol{x}')\,\mathrm{d}\boldsymbol{x}' \approx \frac{V}{N}\sum_{i=1}^{N} f(\boldsymbol{x}_i') \tag{8}$$

where V is the volume of the cube Ω. The result is a convergence rate of $\mathcal{O}\left(1/\sqrt{N}\right)$ independent of dimension.

QMC builds on MC, by selecting samples from a deterministic low-discrepancy sequence rather than a pseudo-random series. A quality low discrepancy sequence, such as the Sobol sequence used here, is designed to cover the space more evenly for a given number of points N. Notably, it can be shown that the QMC convergence rate approaches $\mathcal{O}(1/N)$[12].

QMC is performed over the unit cube with coordinates (u,v,w), requiring a change of variables in equations (4). Consider a body of arbitrary shape contained within its GCS Axis-Aligned Bounding Box (AABB) with vertices $\boldsymbol{X}_{AABB}$. It is straightforward to change variables, rescaling (u,v) in the unit cube to the AABB. Invoking the mathematical definition of the single-valued free surface, the w-coordinate of the unit hypercube is mapped to the z-coordinate of the AABB fluid domain,

$$X = X_{AABB,\min} + u\left(X_{AABB,\max} - X_{AABB,\min}\right) \tag{9a}$$
$$Y = Y_{AABB,\min} + v\left(Y_{AABB,\max} - Y_{AABB,\min}\right) \tag{9b}$$
$$Z\left(X,Y\right) = Z_{AABB,\min} + w\left(\zeta_I\left(X,Y\right) - Z_{AABB,\min}\right) \tag{9c}$$

In order to make an integral over the scaled AABB equivalent to the integral over $\forall_W$, the nonlinear FIT integrands are multiplied by an indicator function $\mathcal{I}_\forall\left(\boldsymbol{X}\right)$ defined in equation (7),

$$\boldsymbol{F}_{Hs}\left(t\right) = \rho g \Delta x \Delta y \iiint\limits_{u,v,w\in[0,1]} \mathcal{I}_\forall\left(\boldsymbol{X}\right)\ \left[\zeta_I\left(x,y\right) - z_{\min}\right] \mathrm{d}w\mathrm{d}v\mathrm{d}u \tag{10a}$$
$$\boldsymbol{I}_{FK,1,2,3}\left(t\right) = \rho \Delta x \Delta y \iiint\limits_{u,v,w\in[0,1]} \mathcal{I}_\forall\left(\boldsymbol{X}\right)\ \left(\nabla\phi_I\right)\left[\zeta_I\left(x,y\right) - z_{\min}\right] \mathrm{d}w\mathrm{d}v\mathrm{d}u \tag{10b}$$

The resulting scaling and sampling is visualized in Figure 3 with 4096 Sobol samples.

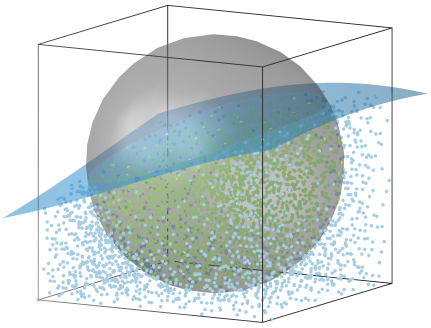

Figure 3: Schematic of 4096 QMC Sobol samples inside the AABB, with green circles representing $\mathcal{I}_\forall = 1$ and blue circles in the fluid domain but outside the body ($\mathcal{I}_\forall = 0$).

2.4 Hyperbolic Tangent Boundary Blur

Moskowitz and Caflisch note that when the integrand is discontinuous, the favorable convergence rate of QMC is often observed to reduce to the convergence rate of MC [13]. As a result, the conditions prescribing the QMC error bound is violated. To mollify the sharp discontinuity at the body boundary and improve the convergence rate of equation (10), equation (7) is exchanged for a continuously differentiable hyperbolic tangent indicator function,

$$\mathcal{I}_s\left(\boldsymbol{p}\right) = \frac{\left(1 + \tanh\left[-\vartheta D_{\mathcal{S}}\left(\boldsymbol{p}\right)\right]\right)}{2} \tag{11}$$

This smooth indicator has the physical effect of blurring the boundary, visualized in Figure 4. The distinct advantage of this framework is the SDF representation, which enables equation

(11) to be evaluated very efficiently. The parameter ϑ corresponds inversely to the "blur thickness" and can be selected to provide a satisfactory compromise between absolute accuracy and convergence rate.

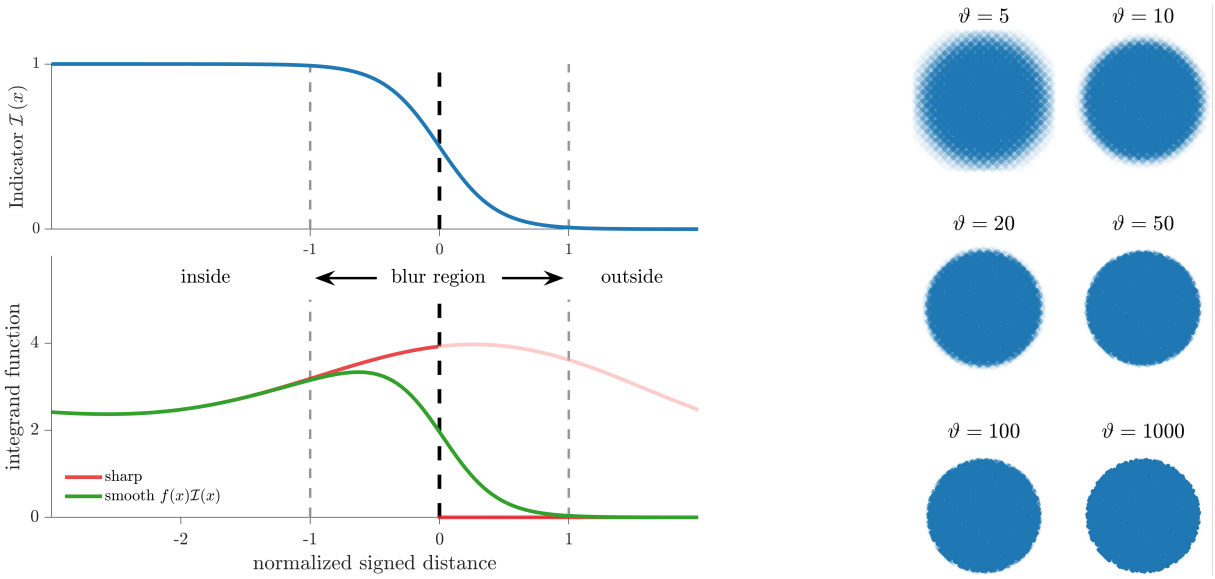

(a) Schematic

(b) 2D illustration

Figure 4: (a) Visual description of hyperbolic tangent boundary blur applied to an integrand function $f(x)$. (b) Visualization of the boundary blur on a 2D circle.

2.5 Impulse-Modified Chebyshev Picard Iteration

Advancing the equation of motion of time is performed by extending the second-order cascade Modified Chebyshev Picard Iteration (MCPI) scheme [14] to equations containing momentum impulses. A key attribute of this method is approximating time-dependent quantities over the Picard interval with a Chebyshev polynomial basis (of the first kind) [15]. Furthermore, Chebyshev polynomials evaluated at the Chebyshev-Gauss-Lobatto (CGL) nodes, $\tau_j = -\cos\left(\frac{j\pi}{M}\right)$, $m = 0, 1, 2, \ldots, M$, exhibit a discrete orthogonality and minimize spurious oscillations due to Runge's phenomenon.

A critical aspect is computing the time-derivative of the nonlinear Froude-Krylov impulse. Integrals and derivatives of Chebyshev polynomials are expressed in terms of the polynomials themselves. The new I-MCPI scheme exploits this relationship to circumvent noise-amplifying finite differences, end-effects and Runge's phenomenon, which when differentiated, may lead to potentially disastrous errors.

To sketch the method, the nonlinear equation of motion containing the FIT nonlinear hydrodynamics over a finite interval $t_0 \leq t \leq t_f$ are expressed as,

$$\ddot{\boldsymbol{x}}(t) = \boldsymbol{f}(t, \boldsymbol{x}, \dot{\boldsymbol{x}}) + \frac{d}{dt}\boldsymbol{I}(t, \boldsymbol{x}, \dot{\boldsymbol{x}}), \quad \boldsymbol{x}(t_0) = \boldsymbol{x}_0, \;\; \dot{\boldsymbol{x}}(t_0) = \boldsymbol{v}_0 \tag{12}$$

where $\boldsymbol{f}$ contains the linear and nonlinear forces and $\boldsymbol{I}$ contains the Froude-Krylov impulse. A change of variables is made to the Chebyshev interval $-1 \leq \tau \leq 1$, letting $t = w_1 + w_2\tau$ with $w_1 = (t_0 + t_f)/2$ and $w_2 = (t_f - t_0)/2$. Applying a change of variables,

$$\boldsymbol{v} = \frac{d\boldsymbol{x}}{d\tau} = w_2 \frac{d\boldsymbol{x}}{dt} \tag{13a}$$

$$\frac{d\boldsymbol{v}}{d\tau} = \boldsymbol{g}\left(\tau, \boldsymbol{x}, \dot{\boldsymbol{x}}\right) = w_2 \boldsymbol{f}\left(t, \boldsymbol{x}, \dot{\boldsymbol{x}}\right) + \frac{d}{d\tau}\boldsymbol{h}\left(\tau, \boldsymbol{x}, \boldsymbol{v}\right) \tag{13b}$$

$$\boldsymbol{h}\left(\tau, \boldsymbol{x}\left(\tau\right), \dot{\boldsymbol{v}}\left(\tau\right)\right) = \boldsymbol{I}\left(w_1 + w_2\tau, \boldsymbol{x}\left(w_1 + w_2\tau\right), \dot{\boldsymbol{x}}\left(w_1 + w_2\tau\right)\right) \tag{13c}$$

Integrating both sides of equation (13b), the velocity and displacement at the i-th Picard update is computed as,

$$\boldsymbol{v}^i\left(\tau\right) = \boldsymbol{v}_0 + \int_{-1}^{\tau} \left\{ \boldsymbol{g}\left(s, \boldsymbol{x}^{i-1}, \boldsymbol{v}^{i-1}\right) + \frac{d}{ds}\boldsymbol{h}\left(s, \boldsymbol{x}^{i-1}, \boldsymbol{v}^{i-1}\right) \right\} \mathrm{d}s \tag{14a}$$

$$\boldsymbol{x}^i\left(\tau\right) = \boldsymbol{x}_0 + \int_{-1}^{\tau} \boldsymbol{v}^i\left(s\right) \mathrm{d}s \tag{14b}$$

using the $i-1$ approximation of the displacement and velocity.

Traditional MCPI fits a Chebychev series to the displacement of order N, a second series of order $N-1$ to the velocity, and a third series of order $N-2$ is fit to the integrand. I-MCPI extends this by also fitting an order $N-1$ Chebyshev series to the nonlinear impulse, noticing it will be differentiated prior to integration,

$$\boldsymbol{x}^i\left(\tau\right) \approx \frac{1}{2}\boldsymbol{\alpha}_0^i T_0\left(\tau\right) + \boldsymbol{\alpha}_1^i T_1\left(\tau\right) + \cdots + \boldsymbol{\alpha}_{N-1}^i T_{N-1}\left(\tau\right) + \frac{1}{2}\boldsymbol{\alpha}_N^i T_N\left(\tau\right) \tag{15a}$$

$$\boldsymbol{v}^i\left(\tau\right) \approx \frac{1}{2}\boldsymbol{\beta}_0^i T_0\left(\tau\right) + \boldsymbol{\beta}_1^i T_1\left(\tau\right) + \cdots + \boldsymbol{\beta}_{N-1}^i T_{N-1}\left(\tau\right)\left(\tau\right) \tag{15b}$$

$$\boldsymbol{g}\left(\tau, \boldsymbol{x}^{i-1}, \boldsymbol{v}^{i-1}\right) \approx \frac{1}{2}\boldsymbol{\gamma}_0^{i-1} T_0\left(\tau\right) + \boldsymbol{\gamma}_1^{i-1} T_1\left(\tau\right) + \cdots + \boldsymbol{\gamma}_{N-2}^{i-1} T_{N-2}\left(\tau\right) \tag{15c}$$

$$\boldsymbol{h}\left(\tau, \boldsymbol{x}^{i-1}, \boldsymbol{v}^{i-1}\right) \approx \frac{1}{2}\boldsymbol{\zeta}_0^{i-1} T_0\left(\tau\right) + \boldsymbol{\zeta}_1^{i-1} T_1\left(\tau\right) + \cdots + \boldsymbol{\zeta}_{N-1}^{i-1} T_{N-1}\left(\tau\right) \tag{15d}$$

The key development is that equation (15d) is analytically differentiated over the Picard interval,

$$\begin{aligned} \frac{d}{d\tau}\boldsymbol{h}\left(\tau, \boldsymbol{x}^{i-1}, \boldsymbol{v}^{i-1}\right) &\approx \sum_{k=1}^{N-1} \boldsymbol{\zeta}_k^{i-1} \frac{dT_k\left(\tau\right)}{d\tau} \\ &= \zeta_2^{i-1}\left(1\right) + \zeta_3^{i-1}\left(\sum_{j=0,\text{even}}^{2} T_j\left(\tau\right)\right) + \zeta_4^{i-1}\left(\sum_{j=1,\text{odd}}^{3} T_j\left(\tau\right)\right) + \ldots \end{aligned} \tag{16}$$

Invoking the discrete orthogonality property, the coefficients of the integrand can be computed independently as,

$$\boldsymbol{\gamma}_k^{i-1} = \frac{2}{M} \sum_{j=0}^{M} \text{“}\boldsymbol{g}\left(\tau_j, \boldsymbol{x}^{i-1}\left(\tau_j\right), \boldsymbol{v}^{i-1}\left(\tau_j\right)\right) T_k\left(\tau_j\right), \quad k = 0, 1, \ldots, N-2 \tag{17a}$$

$$\zeta_k^{i-1} = \frac{2}{M} \sum_{j=0}^{M} \text{“}\boldsymbol{h}\left(\tau_j, \boldsymbol{x}^{i-1}\left(\tau_j\right), \boldsymbol{v}^{i-1}\left(\tau_j\right)\right), \quad k = 1, 2, \ldots, N-1 \tag{17b}$$

where the double prime “ denotes the first and last terms of the summation are multiplied by $\frac{1}{2}$. Substituting equations (15) and (16) into (14a) and (14b) yields the Picard updates in terms of the analytic Chebyshev series,

$$\boldsymbol{v}^i\left(\tau\right) = \sum_{k=0}^{N-1} \text{‘}\boldsymbol{\beta}_k^i T_k\left(\tau\right) = \boldsymbol{v}_0 + \int_{-1}^{\tau} \left[\sum_{k=0}^{N-2} \text{“}\boldsymbol{\gamma}_k^{i-1} T_k\left(s\right) + \sum_{k=1}^{N-1} \boldsymbol{\zeta}_k^{i-1} \frac{dT_k\left(\tau\right)}{d\tau}\right] \mathrm{d}s \tag{18a}$$

$$\boldsymbol{x}^i\left(\tau\right) = \sum_{k=0}^{N} \text{‘}\boldsymbol{\alpha}_k^i T_k\left(s\right) = \boldsymbol{x}_0 + \int_{-1}^{\tau} \left[\sum_{k=0}^{N-1} \text{‘}\boldsymbol{\beta}_k^i T_k\left(\tau\right)\right] \mathrm{d}s \tag{18b}$$

where the single prime ‘ denotes only the first term in the summation is multiplied by $\frac{1}{2}$. By virtue of the integration, differentiation and discrete orthogonality properties of Chebyshev polynomials, these operations to compute the velocity and displacement coefficients $\boldsymbol{\beta}^i$ and $\boldsymbol{\alpha}^i$ may be carried out in a compact matrix form, which has been omitted for brevity, and can be found in [14] for traditional MCPI and [10] for I-MCPI.

Finally, note that the integrand evaluation in equation (18) are only dependent on the previous iteration's position and velocity estimate. Each Picard update then occurs over the finite interval simultaneously. Therefore, the computationally-expensive integrand evaluations may be parallelized to reduce the computation time. Long time record simulations can be computed by partitioning a long record into many short intervals, which are solved sequentially and concatenated together.

3 RESULTS

The I-MCPI algorithm and hydrodynamic response simulation has been implemented in the Julia language using multi-threading in time. The QMC integration is performed via calls to the Cuba library in C [16].

3.1 Convergence of Boundary Blur Error on Volume Integrals

A spatial integration convergence test is performed on the number of QMC samples N and to assess the magnitude of the error induced by the boundary blur on body volume. The performance is assessed on a 4-meter diameter sphere, displayed in Figure 5. The sharp boundary QMC denoted by black circles behaves more erratically for reasonable N, despite achieving the

smallest error with increasing N. Small and moderate values of ϑ (thick blur) converge rapidly to the exact blurred-volume asymptotic error. For moderate blur, $\vartheta R \approx 20$, the error is less than 1% of the true volume. The thickness of the region $0.01 \leq \mathcal{I}_s \leq 0.99$ can be used to estimate a lower bound on ϑ, given as $4.595/\vartheta R \ll 1$, which appears conservative.

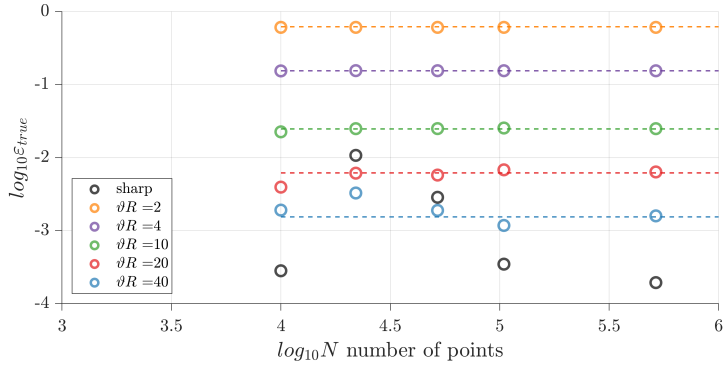

Figure 5: Convergence of the QMC volume estimate of a sphere with boundary blur over various thickness parameters ϑ. The true volume error convergences rapidly to the asymptotic error introduced by ϑ.

3.2 Sensitivity of I-MCPI

A sensitivity study was performed on the I-MCPI algorithm parameters N the polynomial order and Δt the Picard interval length. Simulations were run using a slender circular cylinder with radius 2 meters, draft 8 meters and overall length of 12 meters free to move in heave, with linear hydrodynamics computed by WAMIT, and the linear responses computed using a traditional ODE solver [17]. The response motions in a regular wave of unit amplitude and frequency 0.6 radians per second are shown in Figure 6. For sufficiently short intervals ($\Delta t \leq 1 \implies \Delta t/T \leq 0.1$), the accuracy of the solution appears insensitive to the polynomial order. For $\Delta t = 5, 10$ seconds, the simulation did not succeed. In the context of broader modeling errors, it should be noted that stable simulations can be achieved across broader parameters, while accurate results may require further parameter tuning for a specific problem.

3.3 Long Time Record

To illustrate the stable and robust behavior of the I-MCPI scheme, we simulate a 4 meter diameter heaving sphere for 690 seconds. Figure 7 illustrates the response motions. A 10th-order Chebyshev series was with interval lengths $\Delta t = 1.0$ and $\Delta t = 1.5$ were used. The incident wave is a JONSWAP sea state with a significant waveheight of $H_s = 4$ meters and peak period of $T_p = 12$ seconds. In these conditions, the sphere is expected to behave as a wave-follower and according to Giorgi and Ringwood, linear theory is expected to perform well, providing a useful comparison [**?**]. The new methodology is seen to advance the simulation forward in time in a stable manner, and overlaying the linear theory response motions as expected.

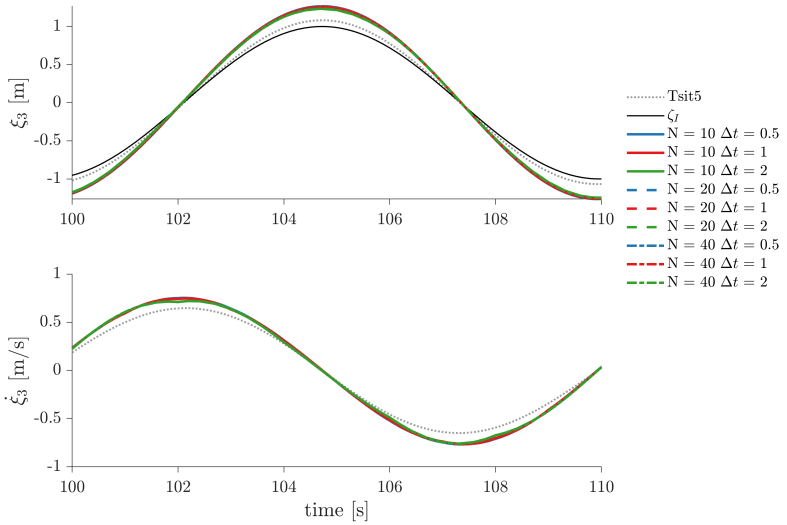

Figure 6: Nonlinear heaving cylinder illustrates I-MCPI is most sensitive to the interval length. Increasing the Chebysehv order appears as coincident response signals.

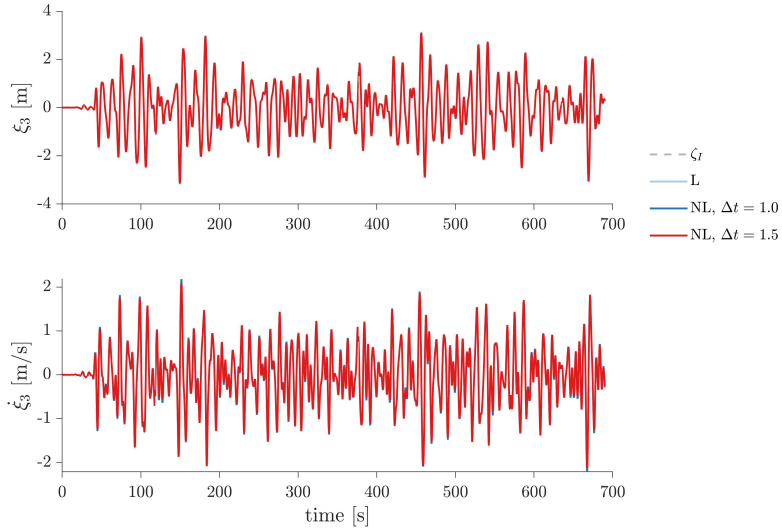

Figure 7: Long time record simulation of a heaving sphere, illustrating the stable behavior of the I-MCPI algorithm and robust evaluation of the nonlinear hydrodynamics.

4 CONCLUSIONS

A new methodology has been introduced to study the nonlinear loads and response motions of floating bodies in irregular waves. An implicit SDF representation, combined with Quasi-Monte Carlo integration algorithms is implemented to evaluate the nonlinear FIT Froude-Krylov and

hydrostatic loads in volume form, enabling arbitrary bodies to be simulated. The critical time derivative of the Froude-Krylov impulse is analytically computed using an extended Chebyshev Picard iteration algorithm, which permits parallel evaluation of the nonlinear equation of motion integrand in time, and may include more complex dynamics, such as the power take off mechanism of a wave energy converter. A boundary blurring smooth indicator function is shown accelerates convergence for moderate values of $\vartheta R \approx 20 - 40$, while keeping the volume error less than 1%. The I-MCPI algorithm is shown to be robust over long time records, with the subinterval length being the more sensitive of the two parameters. While simple geometries were presented in this study, ongoing work is focusing on more complex bodies and wave environments to fully characterize the behavior of the methodology, and extensions to include additional hydrodynamic nonlinearities.

ACKNOWLEDGEMENTS

Support for this work by the U.S. Office of Naval Research (ONR) under Contract N00014-17-1-2985 monitored by Dr. Woei-Min Lin is gratefully acknowledged.

REFERENCES

[1] Davidson, J. and Costello, R. Efficient Nonlinear Hydrodynamic Models for Wave Energy Converter Design — A Scoping Study. *Journal of Marine Science and Engineering* (2020) 8(1):35.

[2] Skorkovská, V., Kolingerová, I. and Benes, B.A. Simple and Robust Approach to Computation of Meshes Intersection. *Proceedings of the 13th International Joint Conference on Computer Vision, Imaging and Computer Graphics Theory and Applications* (2018) pp. 175-182, Funchal, Madeira, Portugal.

[3] Weems, K. and Wundrow, D. Hybrid Models for Fast Time Domain Simulation of Stability Failures. *Proceedings of the 13th International Ship Stability Workshop* (2013) pp. 1-8, Breast, France.

[4] Giorgi, G. and Ringwood, J.V. Analytical representation of nonlinear Froude-Krylov forces for 3-DoF point absorbing wave energy devices. *Ocean Engineering* (2018) 164:749-759.

[5] Bandyk, P.J. and Beck, R.F. The acceleration potential in fluidbody interaction problems. *Journal of Engineering Mathematics* (2011) 70(1):147-163.

[6] Wheeler, J.D. Method for Calculating Forces Produced by Irregular Waves. *Journal of Petroleum Technology* (1970) 22(3):359-367.

[7] Sclavounos P.D. Nonlinear impulse of ocean waves on floating bodies. *Journal of Fluid Mechanics* (2012) 697:316-335.

[8] Cummins, W.E. The Impulse Response Function and Ship Motions. *David W. Taylor Model Basin Research and Development Report* (1962).

[9] Lee, C.H. *WAMIT Theory Manual* Massachusetts Institute of Technolgoy (1995).

[10] Larson, D.F.H. *Quasi-Monte Carlo and Picard Iteration Algorithms for the Nonlinear Hydrodynamics, Dynamics and Controls of Wave Energy Converters*. PhD Thesis, MIT (2021).

[11] Persson, P.O. *Mesh Generation for Implicit Geometries*. PhD Thesis, MIT (2005).

[12] Niederreiter, H. *Random Number Generation and Quasi-Monte Carlo Methods*. SIAM (1992).

[13] Moskowitz, B. and Caflisch, R.E. Smoothness and dimension reduction in Quasi-Monte Carlo methods. *Mathematical and Computer Modelling* (1996) 23(2):37-54.

[14] Macomber, B.D. Enhancements to Chebyshev-Picard Iteration Efficiency for Generally Perturbed Orbits and Constrained Dynamical Systems. *PhD Thesis, Texas A & M* (2015).

[15] Junkins, J.L., Bani Younes, A., Woollands, R.M. and Bai, X. Picard Iteration Chebyshev Polynomials and Chebyshev-Picard Methods: Application in Astrodynamics. *The Journal of the Astronautical Sciences* (2013) 60(3):623-653.

[16] Hahn, T. Cuba—a library for multidimensional numerical integration. *Computer Physics Communications* (2005) 168(2):78-95.

[17] Rackauckas, C. and Nie, Q. Differentialequations.jl — a performant and feature-rich ecosystem for solving differential equations in Julia. *Journal of Open Research Software* (2017) 5(1):15.

[18] Giorgi, G. and Ringwood, J.V. Computationally efficient nonlinear FroudeKrylov force calculations for heaving axisymmetric wave energy point absorbers. *Journal of Ocean Engineering and Marine Energy* (2017) 3(1):21-33.